Implementation of Scheimpflug Lidar for Entomological Monitoring of Bark Beetles

Jonathan Peterson

Supervisor: Mikkel Brydegaard
Co-supervisor: Samuel Jansson

Abstract

Bark beetles are responsible for great damages to Swedish forestry every year. This project focuses on a method of entomological lidar called Scheimpflug lidar to detect and monitor bark beetles. Scheimpflug lidar uses old techniques from photography to achieve a deep field of focus to resolve objects over long distances. Measurements were made in the field as well as in the lab with trapped specimens. Their wing beat frequency was estimated using a parametrization method where their backscattered signals are fitted to harmonic functions. Scheimpflug lidar was also used to detect an ammonium chloride plume to visualize the movement of pheromones in the wind. Finally, using thin film interference from specular bark beetle wing reflections, an estimate of wing thickness was made, which might prove possible to aid in species identification in the future.

Contents

Acronyms

LIDAR	Light Detection and Ranging
WBF	Wingbeat Frequency
NIR	Near Infrared
SWIR	Short Wavelength Infrared
FoV	Field of View
OCS	Optical Cross Section
DoF	Degrees of Freedom

1 Introduction and Background

1.1 Bark Beetles

Bark beetles (*Scolytinae*) are a diverse group of species of weevils evolved to living on and around trees. In Sweden, the European spruce bark beetle (*Ips typographus*) is the insect responsible for causing the most damage to Swedish forestry. During 2018 it was estimated that 3 to 4 million cubic meters of forest was lost to beetle infestations. This is considerably more than the estimated 2 million cubic meters lost in the many forest fires that summer and its damages costs billions of SEK each year [1, 2].

The beetles mainly target storm-fallen trees but also living ones, especially if the trees are stressed or weakened by drought. The beetles can pick out stressed host plants by olfactory signs but may even infest healthy ones if the concentration of beetles is high enough. After a male has landed, he communicates using pheromones to attract other conspecifics of both sexes as he burrows into the bark. There he awaits a female as he hollows out a small mating chamber. The females are attracted using pheromones and after mating, the female digs further tunnels where she lays her eggs. After hatching, the larvae in turn dig their own tunnels perpendicular to the original one. They keep burrowing as they feed, leading to wider tunnels ending in an exit. The larvae take approximately 10-12 weeks to mature into beetles, ready to leave the tree. If conditions are right, they might move on to another, leading to multiple swarming events in a single year. Otherwise they burrow underground and hibernate awaiting warmer weather. In the spring, the temperature needs to rise to approximately 18 °C before the beetles start to submerge [3].

Figure 1.1: *Bark beetle caught in Nyteboda under a microscope.*

Figure 1.2: *Holes and tunnels dug by bark beetles in a spruce in Nyteboda.*

The best way to protect a forest from major outbreaks is by removing wind-fallen trees as well as trees with clear signs of invasion in between swarming events. To track the spread and outbreak of bark beetles in Swedish forests, each year traps are placed in areas with high predicted or observed activity. Pheromone traps are both used as pest control and as a tool to monitor the number of beetles in an area [4]. Like all insect traps, pheromone traps are subject to bias and possess low temporal resolution, usually on the

order of hours. It is also difficult to estimate the range as pheromone dispersal depends on local wind conditions and might change over the course of a day. A noninvasive, nonbiased monitoring method with higher temporal and spatial resolution would be preferred to get a clearer picture on bark beetle activity in a single area.

1.2 Scheimpflug Lidar

Light detection and ranging (lidar) is a remote sensing technique similar to the older, well known radar from which it received its name. But unlike radar, lidar uses intense, collimated light beams, such as from a laser, instead of microwaves, to illuminate a target [5]. Today lidar has numerous applications in studies of the atmosphere, for example to measure atmospheric gases, aerosol particles and flying insects [6].

In this work, a particular method of lidar called Scheimpflug lidar has been used. Scheimpflug lidar is a remote sensing method developed at Lund University based on two established conventions of photography: The hinge rule and the Scheimpflug condition [7]. In combination, these two rules relate five planes to two lines and allow for a deep field of focus with short exposure times. For most instances of imaging, for example photography, the lens plane is parallel to the plane of the subject being imaged. This places the image plane of focus in the same orientation and a detector, such as a CCD detector in a camera, can also be placed parallel with the lens and object planes. This has the drawback that only a small region of depth comes into focus. One way of mitigating this is to have a smaller light-gathering aperture, such as in a pinhole camera, which allows for a deeper field of focus. This, however, reduces the amount of light reaching the detector and longer exposure times are usually required placing restrictions on movements of the subject. Figure 1.3 shows a comparison between images taken from a train using these three different techniques.

Figure 1.3: *Comparison between conventional, pin hole and Scheimpflug photography on images taken from a train. Image credit Malmquist et al. [8].*

Figure 1.4 shows the two rules in practice as they appear in photography. The Scheimpflug rule states that the image plane, the lens plane and the plane of focus need to coincide on the Scheimpflug line. Adhering to the Scheimpflug rule does however not ensure that the image is in focus as the plane of focus rotates about the Scheimpflug line depending on the focal length of the lens. This is accounted for by applying the Hinge rule. The Hinge rule states that the parallel-to-image lens plane and the front focal plane of the lens need to coincide with the plane of focus on a line called the hinge line. By fulfilling this, the plane of focus will be on the image plane.

Applying these rules to lidar translates to the laser illuminating along the plane of focus so that anything appearing inside the laser beam is in focus and everything outside
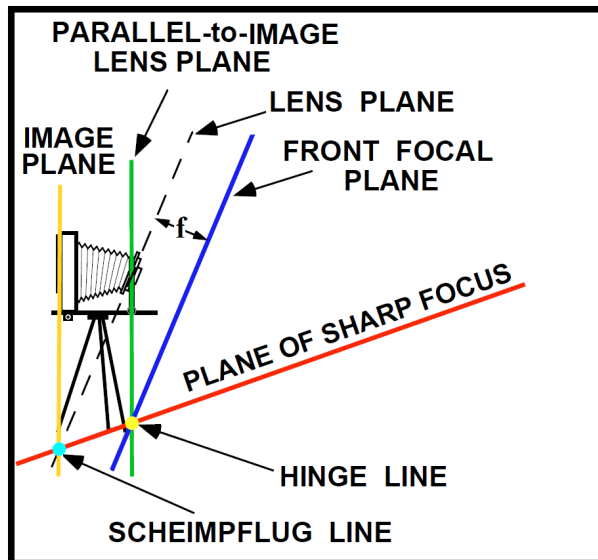
Figure 1.4: *Scheimpflug and Hinge rules. Image modified from Merklinger [9].*

it is not. The detector plane and the lens plane then cut the plane of focus at the Scheimpflug intersection. Figure 1.5 shows a depiction of this.
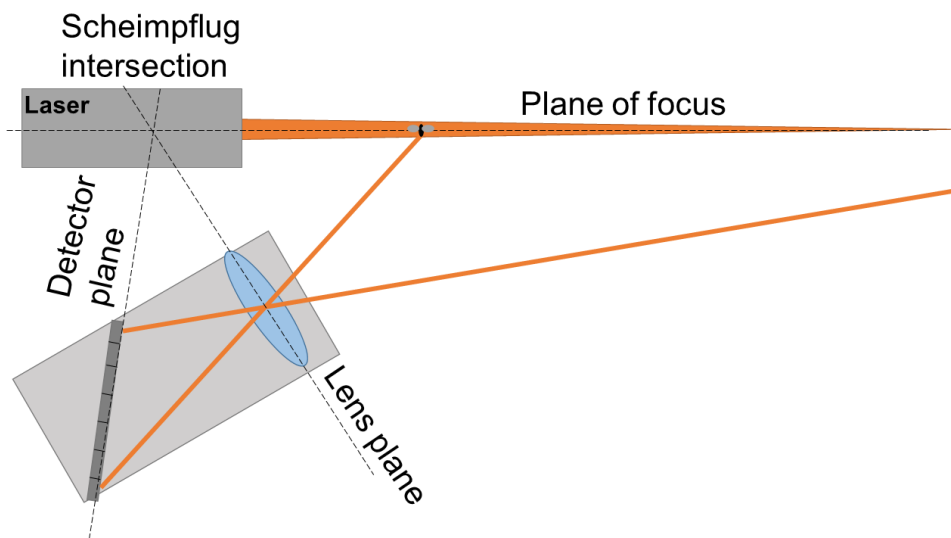

Figure 1.5: *Graphic of Scheimpflug lidar with insect at near limit.*

The pixel on the detector that the light focuses on then relates to a distance the object was illuminated at where the first pixel is focused at infinity. Figure 1.6 shows this nonlinear relation. Scheimpflug lidar has the advantage compared to time-of-flight lidar that it can be implemented with compact, high power, continuous wave laser diodes [10].
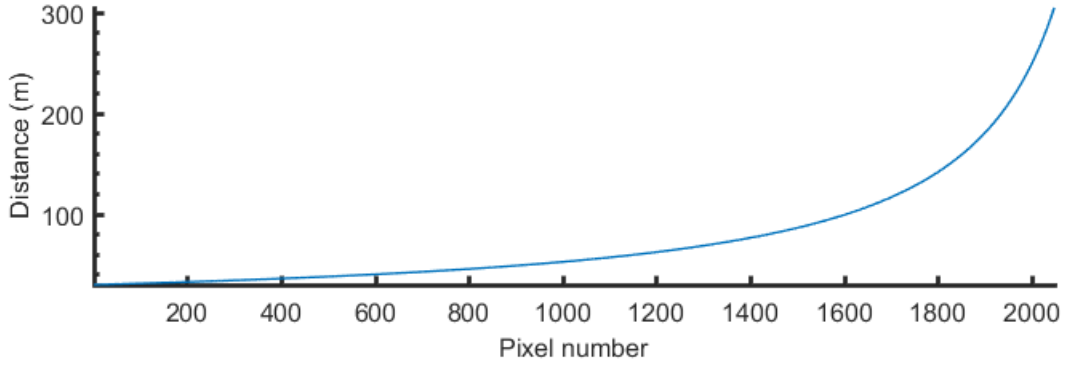
Figure 1.6: *The relationship between pixel number and object distance for detection with Scheimpflug lidar.*

1.3   Beetle-light interactions

Beetles have two sets of wings: forewings (*elytra*) and hindwings. The hindwings are thin, clear, elastic and used for flight [11]. They are folded up on the back of the abdomen, protected by the forewings, when the beetle is grounded [12]. Figure 1.7 shows a pinned bark beetle captured in Nyteboda with its hindwings extended. The hindwings consist of long chains of polysaccharide biopolymers, called chitin [13].
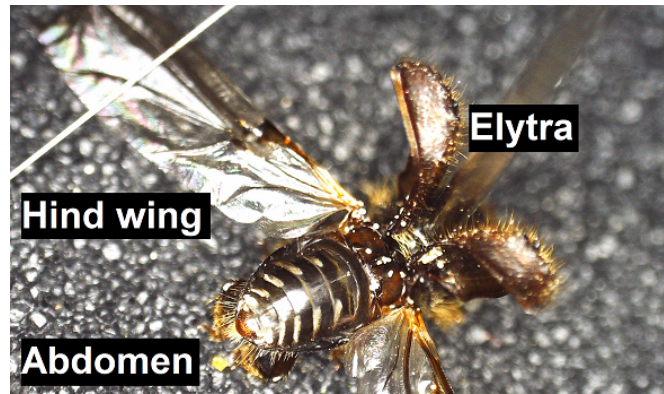

Figure 1.7: *Pinned bark beetle with wings extended.*

Reflected light of a flying insect can be divided into two temporal components: an envelope mostly produced by the body, and an oscillating part produced by the beating wings. Light reflected of the wings oscillates with the fundamental wing beat frequency (WBF) which varies between certain species and can be used for species identification [14]. The reflection from the body can either be from the surface, in which case it is specular, or penetrate into the inner layers where it undergoes absorption and multiple scattering. The reflection from the wings will vary depending on the wing normal with respect to the light. Because the wings are clear they can give rise to thin film interference, with chitin having an average refractive index of $n = 1.56$ for wavelengths around the visible spectrum [15, 16, 17]. The condition for constructive interference is given by:

$$\lambda_{max} = \frac{2nd}{m - \frac{1}{2}}, \quad m \in N$$

where λ_{max} is the wavelength, d is the thickness of the wing and m is an integer.

6

2 Experimental Setup
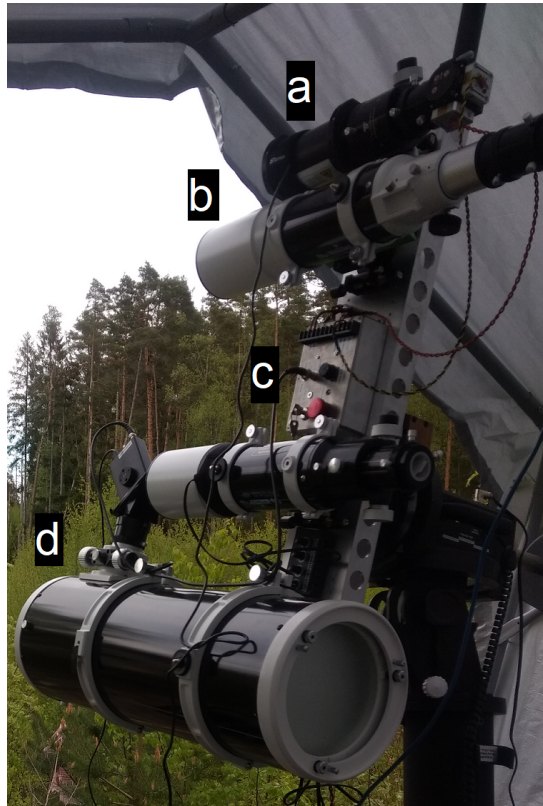
2.1 Entomological lidar

Figure 2.1: *Image of lidar setup in Nyteboda. a) Laser transmitter. b) Monitor camera c) Driver d) Receiver telescope.*

The lidar setup used in Nyteboda was installed on a motorized telescope mount. Figure 2.1 shows a picture of it used in the field. It had a 5 W, 808 nm laser diode transmitted through a 3 inch expander. The backscatterd light was collected by a Newtonian telescope, with a diameter of 205 mm and a focal length of 800 mm, onto a CMOS line array sensor tilted 45 degrees compared to the axis of the telescope. The baseline separation distance between the laser and the receiver was 814 mm. They were operated by a driver in a sequence where the laser was intermittently turned on and off to allow for background measurements. In between the receiver and transmitter, there was also a monitoring camera connected to a refractor telescope viewing the beam termination to aid focusing.

2.2 Entomological test chamber

The entomological test chamber was a small enclosed chamber in which insects were free to fly around and could be illuminated by two overlapping laser beams. The two lasers were overlapped with a beam splitter and expanded to have a beam diameter of 50 mm. The beams were transmitted through a small hole into the chamber and terminated at the far end. The beams were produced by two laser diodes with wavelengths 808 and 1550 nm with a maximum output of 5 and 3 W, respectively. The beams had an overlap, inside the test chamber, with the field of view of two photo-diodes used to measure the backscattered light of insects flying through the beams with a sampling frequency of 20 kHz. The backscattered light was split by a polarization beam splitter so that one photodiode only measured co-polarized and one only measured de-polarized light. The photodiodes were sandwiched Silicon and Indium Gallium Arsenide to detect the backscattered intensity from the 808 and 1550 nm lasers, respectively. Figure 2.2 shows a drawing of the geometry.
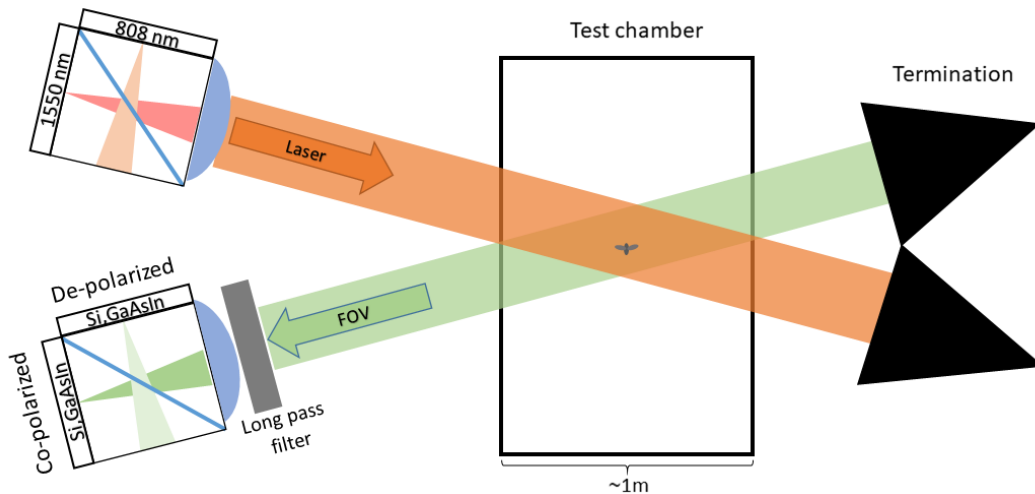

Figure 2.2: *Graphic of entomological test chamber setup.*

The bark beetles were placed in a cup directly underneath the laser beam with edges to steep to crawl over and as such could only exit by flying. To simulate day time conditions two DC powered white LEDs were used to illuminate inside the chamber and a space heater was used to raise temperature and stimulate flight.

3 Data analysis

3.1 Lidar file processing

The lidar data are recorded as 16-bit intensity count values on each of the 2048 detector pixels and a new set of values are recorded on every time-slot as set by the update frequency, in this example set to 3.6 kHz. One file, referred to as a frame, contains 10 seconds of measurements. The frames are read into matlab as matrices and contain 2048x36000 elements, each a 16 bit unsigned integer representing the measured intensity. The time slots follow the sequence set by the driver where the laser is intermittently on and off to measure background. The background measurements can be seen as lower intensity every other time slot. The background is accounted for in each on slot by subtracting the mean of two neighbouring background slots giving a new 2048x18000 element matrix. Figure 3.1b shows an example of this measured in Nyteboda with the termination visible in the uppermost part.
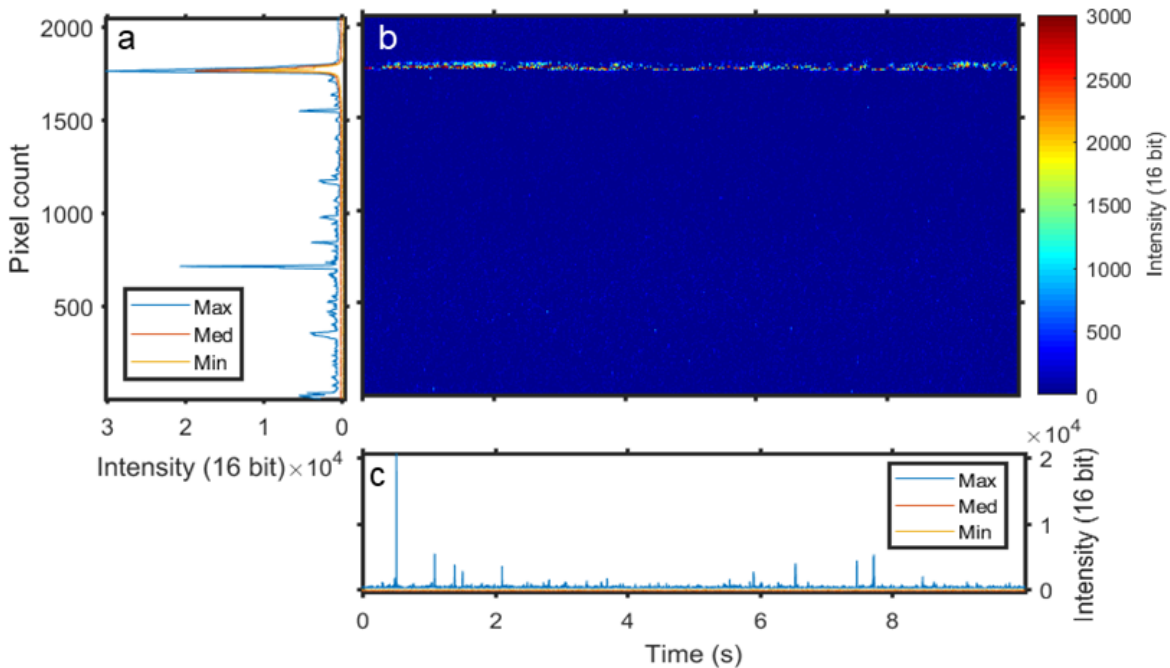

Figure 3.1: *a) Maximum, median and minimum values by pixel from the frame in b. b) Background subtracted frame. c) Maximum, median and minimum values by time slot from the frame in b.*

To characterize insect observations statistics from each row and column is collected. Figure 3.1a,c shows the maximum, minimum and median values in range and time respectively. A region of interest is defined a few pixels away from the termination to because of the strong signal it reflects, which can be seen in figure 3.1a. This makes intensities backscattered by insects the maximum values, as seen in 3.1c .

3.2 Lidar OCS calibration

The intensity pixel values are calculated to equivalent optical cross section (OCS) as performed by Brydegaard *et al.*[18, 19]. OCS is calculated in units of area (mm^2) by comparison with the termination board which is given by:

$$\sigma_{term} = R_{term} * W_{term} * H_{term}$$

where R_{term} is the reflectivity of the neoprene on the termination board, W_{term} and H_{term} are width and height of the probe volume at the termination, respectively. The probe volume is the volume both illuminated by the laser and inside the field of view of the detector and is where insects can be detected. The laser beam and detector field of view (FoV) are both calculated in terms of width and height as functions of range. The probe volume dimensions are given by the overlap of the detector field of view and the laser beam. σ_{term} can then be used to convert the entire matrix into equivalent OCS values at different ranges r:

$$\sigma_{insect} = \frac{\sigma_{term} * r_{insect}^2}{r_{term}^2}$$

3.3 Lidar insect observations

To define what constitutes an insect observation a threshold value is defined for each pixel row in each frame. To determine a threshold value, a histogram of all recorded values in one pixel over the course of one frame is created, as can be seen in figure 3.2. The threshold value is then defined as 5 times the interquartile range of the histogram. Figure 3.3b shows an example with the threshold value compared to intensities produced by an insect.
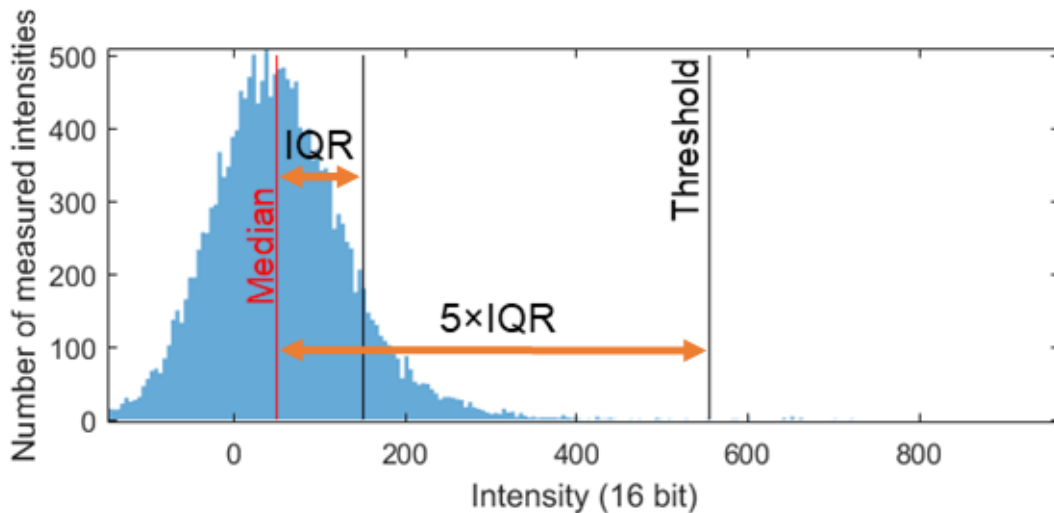

Figure 3.2: *Histogram of recorded intensities in one pixel. The threshold for observations is defined as 5 times the interquartile range.*

The position of pixels with values above the threshold are then recorded as ones in a binary mask with the same dimensions as the original data matrix. To further sort the possible observations the mask is passed through two image masks. The first erodes observations smaller than 1 pixel × 3 time samples which are deemed too small, as to not include possible observations with too little information. The second mask dilates the

number of pixels around an observation to at least 5 pixels × 30 time samples to include information around the times when the threshold intensity was reached. Dilation also ensures that no observation is counted twice which might otherwise happen due to the oscillatory behaviour of the reflected light. To study the oscillatory behavior the range pixels intensities in one observation are summed over each time slot. Figure 3.3d shows the summed time series from the observation above it.
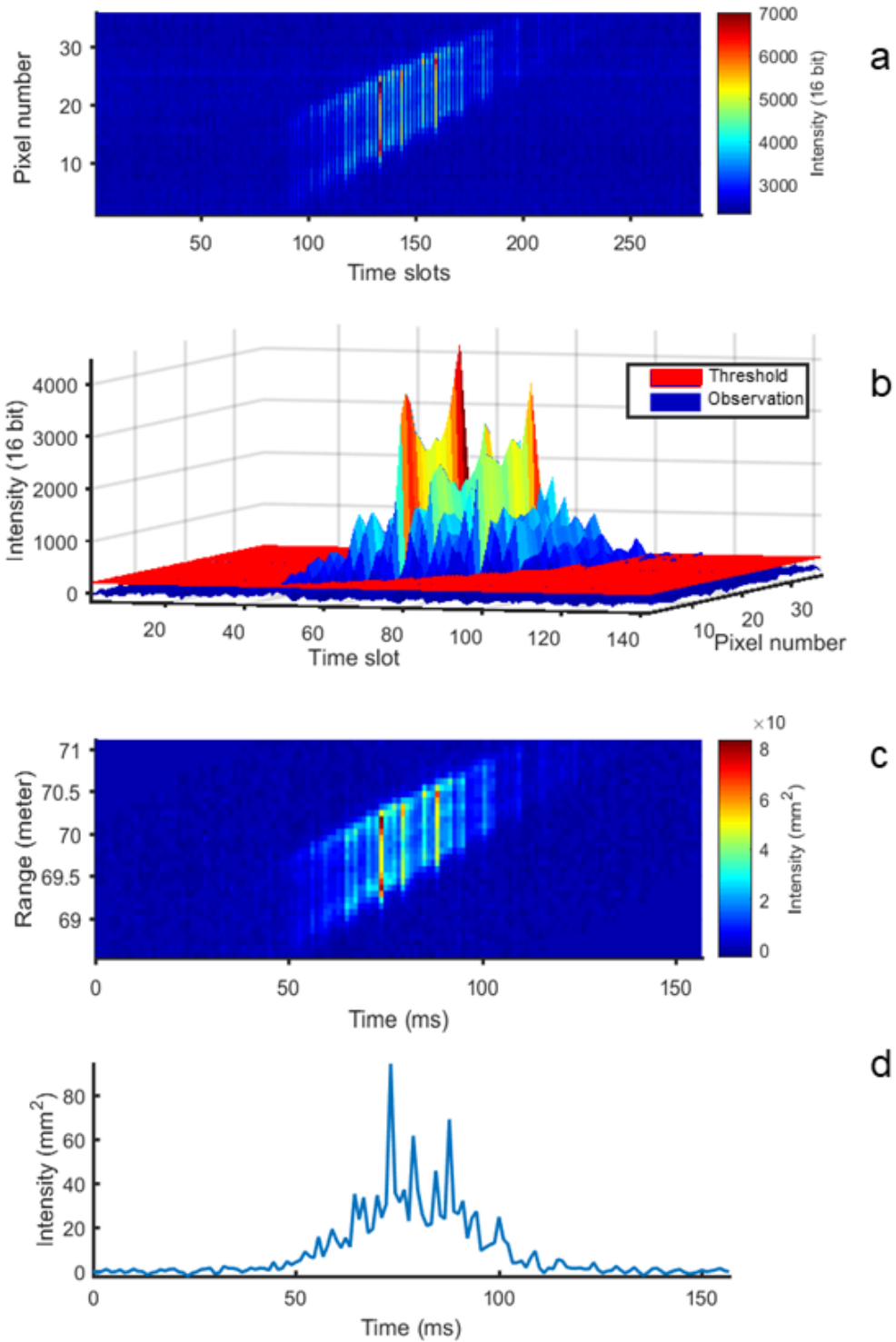
Figure 3.3: *Various steps in the process of defining an insect observation. a) Raw data excerpt showing an insect observation in time slots and pixel number. The background measurements can be seen as lower intensity every other time slot. b) Thresholding of "laser on" slots to define the insect observation. c) Observation in time, distance and OCS. d) Time series summed over all range slots in the observation.*

3.4   WBF determination

The method used in this project to find the fundamental WBF of insect signals tries to minimize the residual between a set of harmonic functions and the time series of an insect observation. The method is described in [20, 21]. A vector of test frequencies is created ranging from a maximum, normally the Nyquist frequency $f_{max} = \frac{fs}{2}$, down to a suitable lower bound, normally the lowest possible frequency where 3 wing beats can be contained by the signal: $f_{min} = \frac{3}{\Delta t}$ where Δt is the length of the signal.

To test the range of frequencies, the signal needs to be divided into two parts: an oscillatory part resulting from the wing beats and a body part resulting from reflected light of the body. To do this, a time window is defined as:

$$ W = \frac{f_s}{f_{test}} $$

rounded to the nearest integer, where f_{test} is the current frequency being tested and f_s is the sampling frequency. The reason the window is defined this way is that the size of the window is approximately one wing beat period for the current test frequency. The window is used to produce an envelope of the signal by taking the average of the window as a sliding minimum and maximum. The envelope is then smoothed by convoluting it with a Gaussian. A regressor of harmonic functions is then created to the order:

$$ n_i = 1, 2, 3, ... n_{max} = 1, 2, 3... \lfloor \frac{f_N}{f_{test}} \rfloor $$

where the integer n_{max} is the highest order of harmonic in the regressor, as this is the highest harmonic that can be resolved for the test frequency f_{test}. The number of columns in the regressor thus becomes:

$$ n_{columns} = 1 + 2 n_{max} $$

which are the degrees of freedom (DoF) of the regressor. Each row in the regressor corresponds to one time slot t_i in the original signal. These are then weighted by their corresponding envelope values: b_i to produce a better fit. The resulting regressor matrix R becomes:

$$ \begin{vmatrix} b_1 & b_1 \sin\left(2\pi n_1 f_{test} t_1\right) & b_1 \cos\left(2\pi n_1 f_{test} t_1\right) & ... & b_1 \cos\left(2\pi n_{max} f_{test} t_1\right) \\ b_2 & b_2 \sin\left(2\pi n_1 f_{test} t_2\right) & b_2 \cos\left(2\pi n_1 f_{test} t_1\right) & ... & b_2 \cos\left(2\pi n_{max} f_{test} t_2\right) \\ b_3 & b_3 \sin\left(2\pi n_1 f_{test} t_3\right) & b_3 \cos\left(2\pi n_1 f_{test} t_1\right) & ... & b_3 \cos\left(2\pi n_{max} f_{test} t_3\right) \\ \vdots & \vdots & \vdots & \vdots & \vdots \\ b_{end} & b_{end} \sin\left(2\pi n_1 f_{test} t_{max}\right) & b_{end} \cos\left(2\pi n_1 f_{test} t_{max}\right) & ... & b_{end} \cos\left(2\pi n_{max} f_{test} t_{max}\right) \end{vmatrix} $$

and to find the coefficients of the regressor, linear regression is used to solve the least squares problem with QR factorisation:

$$ C = (R^T R)^{-1} R \sigma $$

where C are the coefficients and σ is the signal. A reconstructed signal is then produced using the coefficients:

$$ \hat{\sigma} = R * C $$

To find the WBF a residual $e_{initial}$ for each frequency is produced by subtracting the reconstructed time series from the original times series and taking a sum of squares over all time slots:

$$e_{initial} = \sum (\sigma - \hat{\sigma})^2$$

The frequency with the minimum residual is accepted as the fundamental WBF.

Frequency biasing

The parametrization method is biased towards lower and higher frequencies due to the DoF in the envelope and regressor. Two methods to compensate for this were used as described in Jansson *et al.* [22].

When the DoF of the regressor increases the residuals decrease as a function with higher harmonics describe a signal better in general. This occurs for lower frequencies as:

$$n_{max} = \lfloor \frac{f_N}{f_{test}} \rfloor$$

To compensate for this, an analytical function describing the behavior based on the DoF is constructed:

$$e_{reg} = 1 - \frac{DoF_{reg}}{L}$$

where L is the length of the signal. The function is then divided from the total residual.

The DoF of the envelope are given by:

$$DoF_{envelope} = \frac{L}{W}$$

which increases for higher test frequencies as the window gets shorter. When the DoF of the envelope increases the initial residual $e_{initial}$ also decreases. This can be thought of as the weighting from the envelope almost depicting the original time series as the window size decreases. To compensate for this an error vector $e_{envelope}$ is created as the RMS error of the envelope and the original signal and is also divided with the total residual. The resulting compensated residual becomes:

$$e_{comp} = \frac{e_{initial}}{e_{envelope} * e_{reg}}$$

3.5   Chamber OCS calibration

The optical cross section for insects in the entomological lidar test chamber are calibrated against small white Teflon balls (*rgpballs* [23]). The balls are matte and their reflection is estimated to be lambertian. The balls were dropped through the laser beam at the same distance as the cup of bark beetles was set up. To convert the intensity values into OCS, the average of the max intensities of 3 reference measurements is considered the intensity equivalent of the OCS of the ball.

Figure 3.4: *OCS calibration ball on a metallic background.*

3.6   Chamber Observations

The method used to determine insect observations from the test chamber was similar to the lidar method described in previous sections. The raw data was collected in four 10 second vectors, two in each wavelength for each of the two polarizations (co-polarized and de-polarized). The co-polarized light retained the polarization of the laser and the depolarized had a polarization direction perpendicular to the co-polarized. The median in each vector was then subtracted as background and a threshold of 5 times the interquartile range was defined. A binary mask was defined, with the same number of elements as the original vector, with ones for values surpassing the threshold and all other elements as zeros. The mask was then eroded for strings of ones shorter than 10 elements, meaning they were switched to zeros. Finally the remaining strings of ones were dilated to include information before and after the insect surpassed the threshold. The positions of the remaining ones in the mask were defined as insect observations in the original vector.

The observations collected in the flight chamber contain light collected from both the beating wings and the body of the insect being illuminated by the laser, and can be seen as a sum of the two. Figure 3.5a shows an example of an observation. To distinguish the body contribution from the observation, a sliding minimum approximately one wing beat period in window size, is used. The sliding minimum window moves through the vector one element at a time and creates a new vector with the minimum values contained within the window. This operation can be seen in figure 3.5b. The result of the sliding minimum is then convoluted with a Gaussian to smooth it. An example of this convolution is shown in figure 3.5c. A comparison between the original signal, the sliding minimum and the smoothed minimum and be seen for the two 808 nm channels in figure 3.5d. The body contribution is then subtracted from the signal to reduce it to the wing contribution.

Once the wing contribution has been generated, it can be further reduced into specular and diffuse contributions. The reasoning behind the method used is that a specular reflection is only seen when a co-polarized signal reaches its maximum, as the maximum is reached when the wing is perpendicular to the laser beam. By subtracting a de-polarized channel from a co-polarized channel, adjusted for the difference between diffuse and specular reflections, the difference will be the specular reflections in the co-polarized channels. The adjustment is made by taking the ratio between a de-polarized and co-polarized channel at times when there is no specular reflection. Figure 3.5e shows the 808 channels with the specular component having been subtracted from the copolarized channel. Figure 3.5f shows only specular reflections in both laser channels [24, 25].
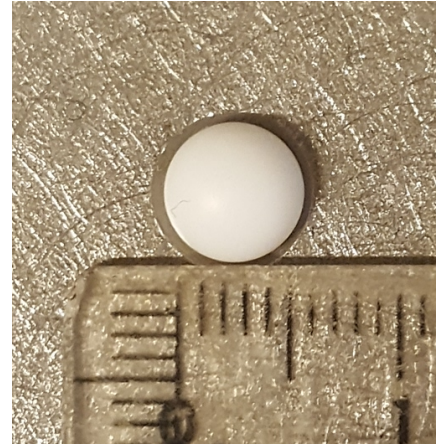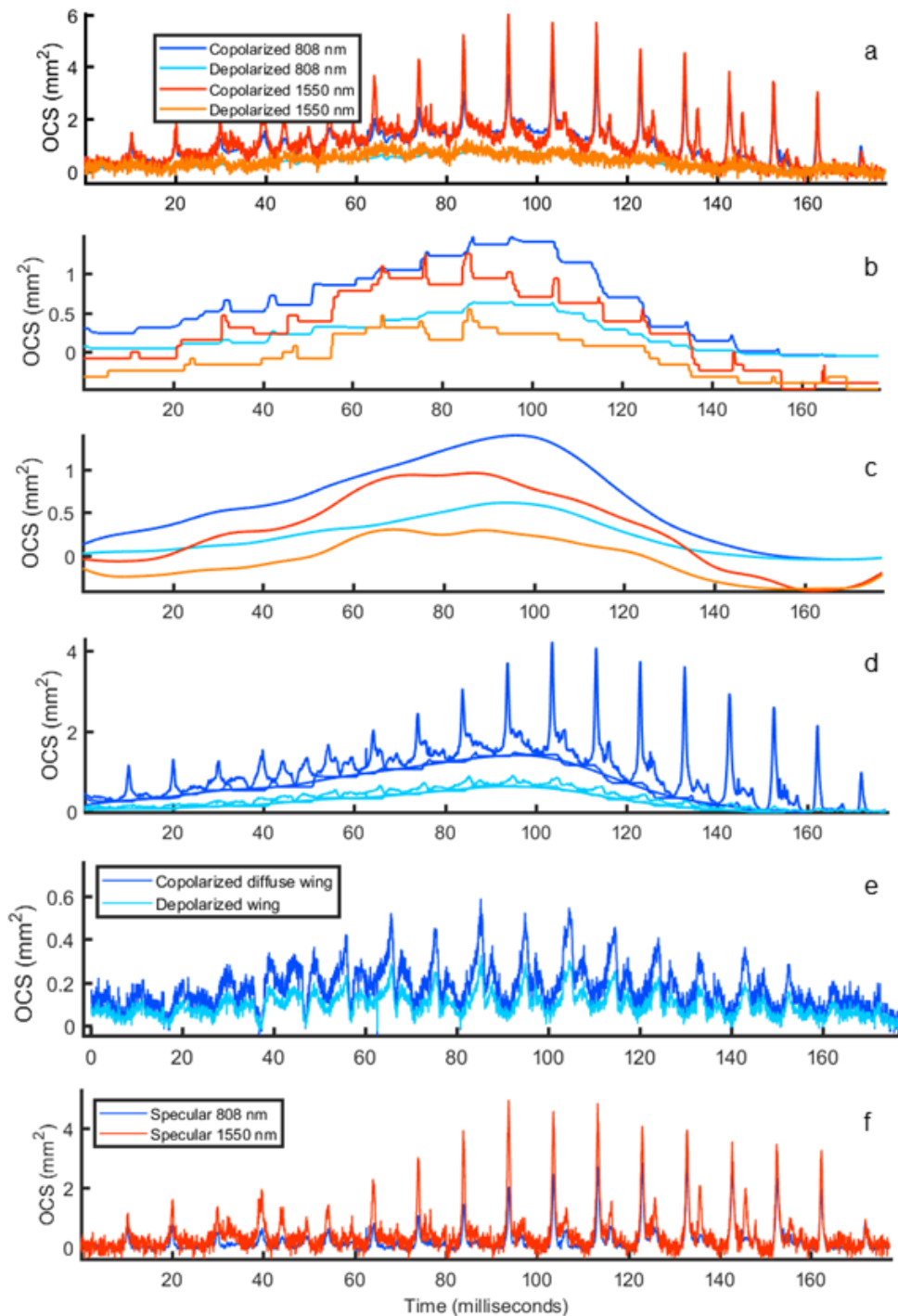
Figure 3.5: *Shows various steps in the analysis of a bark beetle observation in the test chamber. The channels keep their color coding throughout the figure. a) An observation in all four channels calibrated into OCS (mm²). b) A reduction to body part by sliding minimum. c) Same as in b but convoluted with a Gaussian. d) Comparison between original signal, sliding minimum and smoothed minimum in the 808 nm channels. e) Diffuse wing reflections in the 808 nm channels. f) Specular reflection in both 808 and 1550 nm.*

4 Nyteboda Campaign

The Nyteboda campaign was undertaken between May 13 and May 17, 2019. It was based in Nytebodaskogen, a nature reserve next to a cattle farm. The Scheimpflug lidar system was set up under a tent on a small hill next to a barn which can be seen in figure 4.1 and the transect was over a small clearing in a valley and terminated on a beech tree further into the forest. Directly underneath the transect, a pheromone trap was set up to lure bark beetles. A weather station was also set up to record ambient conditions. In
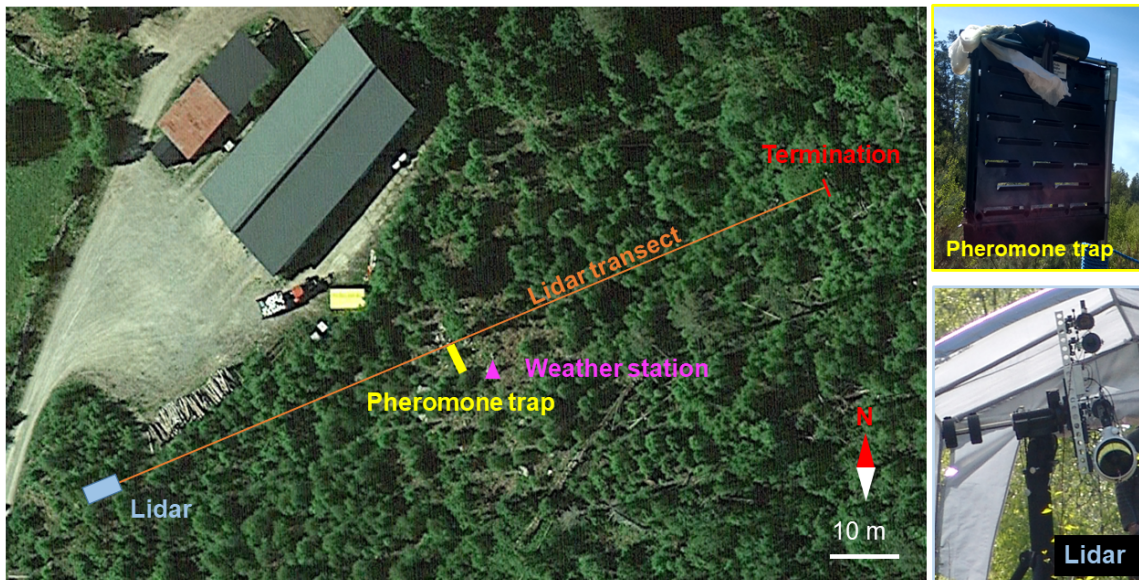
Figure 4.1: *Map over lidar transect in Nytebodaskogen*

an effort to visualize the movements of the otherwise invisible pheromones, a chemical mixture of hydrochloric acid and ammonia, producing an ammonium chloride plume, was placed on to of the bark beetle trap for one hour on May 16th. Ammonium chloride, also known as salmiak, is commonly used as a flavouring in salty licorice [26]. The temperature was initially too low to have bark beetle swarming and it was only on the last day that beetles were caught in significant numbers. Figure 4.2 shows the temperature over the last three days of the excursion. Using the trapped beetles a release directly underneath the transect was possible to obtain reference measurements of bark beetles. Some of the trapped bark beetles were also brought back to Lund to be used in the entomological test chamber.
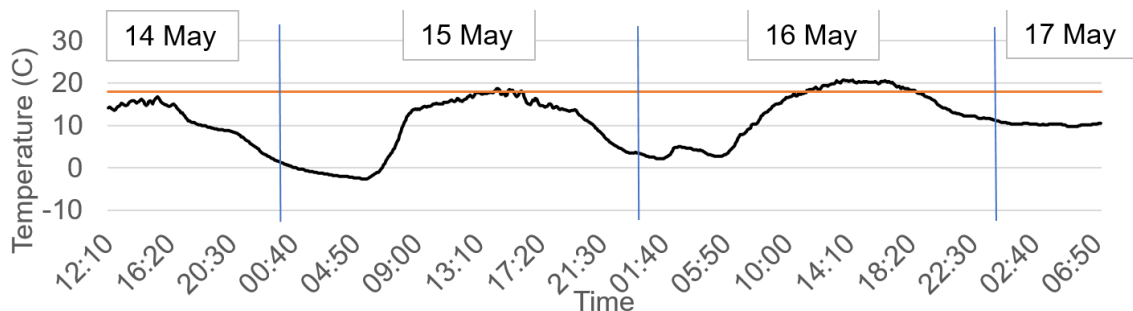

Figure 4.2: *Temperature over a three day period during the Nyteboda campaign. The orange line shows 18 degrees C at which bark beetles become active.*

5 Results and Discussion

5.1 Bark beetle WBF determination

To calculate the wing beat frequency, observations collected in the test chamber were analyzed using the parametrization method described in the data analysis section. 12 observations were chosen based on their length, noise level and number of wing beats present. These observations laid the basis to find a span of WBFs used to find the observations of possible bark beetles. Figure 5.8 shows a bar plot of the determined frequencies with
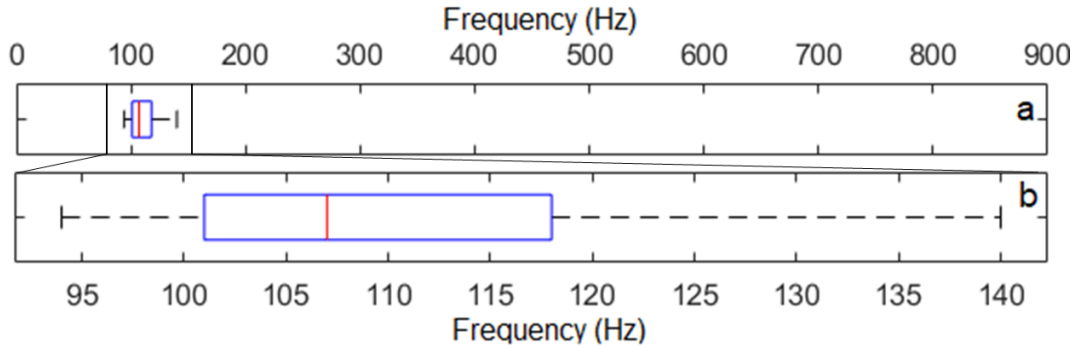

Figure 5.1: *Bar plot of measured WBFs in the entomological test chamber. a) Shows the frequency span up to the Nyquist frequency 900 Hz. b) Shows an excerpt of the spectrum around the measured frequencies.*

a span ranging from approximately 95 to 140 Hz. WBFs in some insects can, however, vary as much as 50% based on external factors such as temperature, humidity and time of day [27]. As the conditions in the test chamber were different it is not certain that this span represents the WBFs that were present during field conditions.

5.2 Bark beetle detection

Figure 5.2 shows an observation presumed to be a bark beetle based on range and time during the release of trapped bark beetles. A calculation based on the time between wing beats shows a fundamental frequency of approximately 135 Hz.
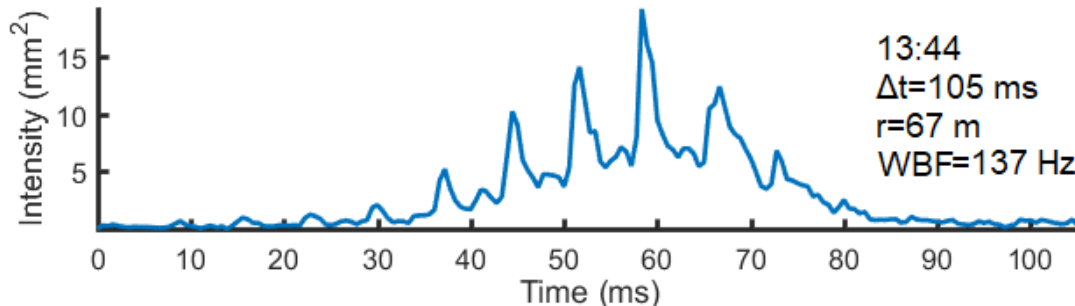

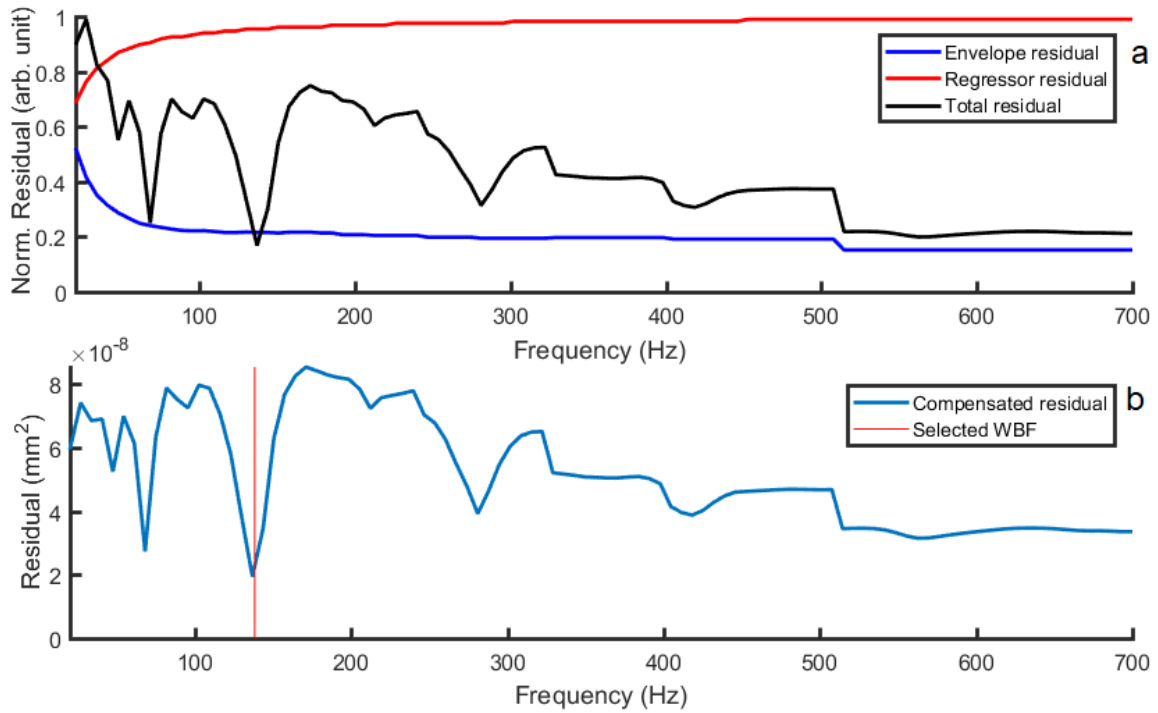Figure 5.2: *Lidar signal of an observation presumed to be a bark beetle.*

Figure 5.3: *Residual curves as function of test frequency after applying the parametrization method to the observation in figure 5.2. a) Shows normalized residual curves of the initial residual and the two compensation functions. b) Shows the total residual after compensation by the envelope and regressor functions.*

Figure 5.3a shows the residuals of the observation in figure 5.2 before compensation. The WBF of bark beetles lie in the lower end of the spectrum but the uncompensated residual function still might choose one in the higher range due to decreasing size of the window. The step like behavior originates from the window size shrinking in integer steps as the test frequency decreases. As can be seen in the 5.3b the compensated residual chooses the right frequency.
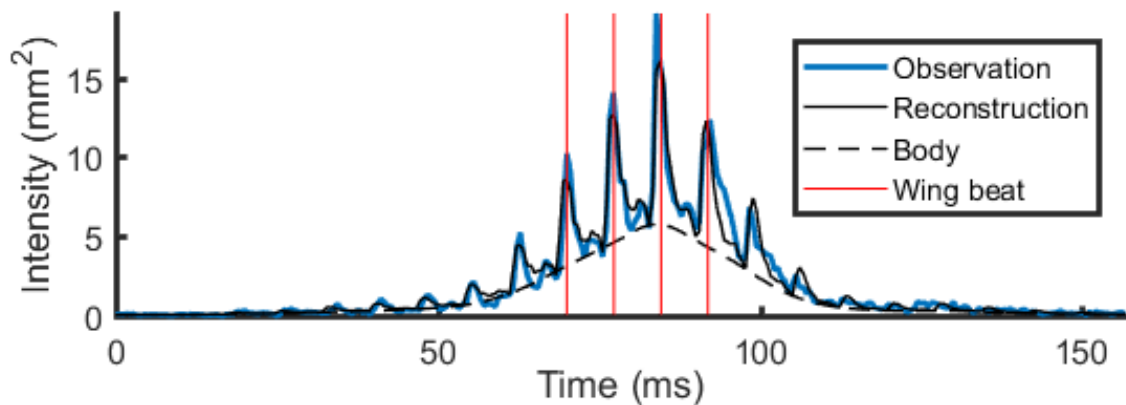

Figure 5.4: *Reconstruction compared to original signal as well as wing beats with a period given by the parametrization method.*

Figure 5.4 shows the reconstructed signal $\hat{\sigma}$ given by the parametrization model in comparison to the original signal. The wing beats were placed by matching the first

one with a peak in the original signal and then spaced with the period suggested by the parametrization model which match well with the original signal.
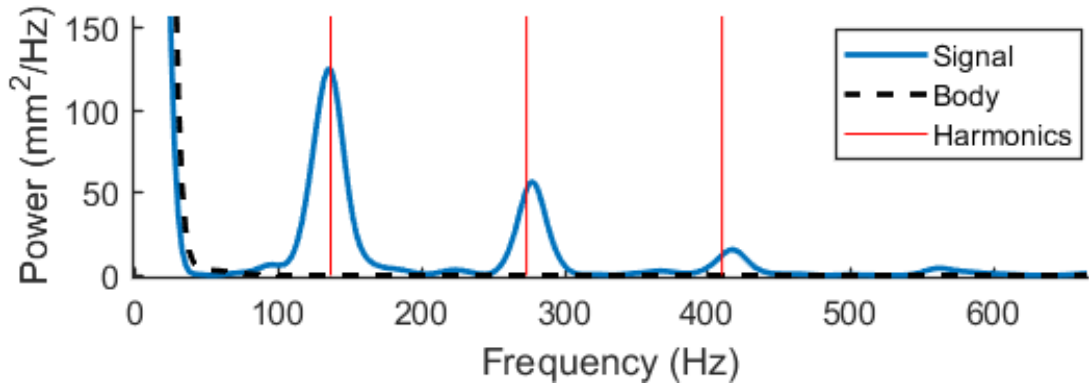

Figure 5.5: *Power spectrum of the time series and the body contribution. The red lines indicate the selected WBF and its overtones.*

To visualize the frequencies present in the original signal, figure 5.5 shows a power spectrum. The marked frequencies are the WBF and its overtones as selected by the parametrization model.

Observation sorting

To measure three wing beat periods of the lowest frequency in the selected bark beetle WBF span (95 Hz) the shortest transit time is given by:

$$\frac{3}{95\,\mathrm{Hz}} = 31.6\,\mathrm{ms}$$

and observations shorter than this were sorted out of the parametrization method. Figure 5.6 shows a histogram of transit times over one hour with the shortest transit time marked to give an estimate of how many observations are sorted out.
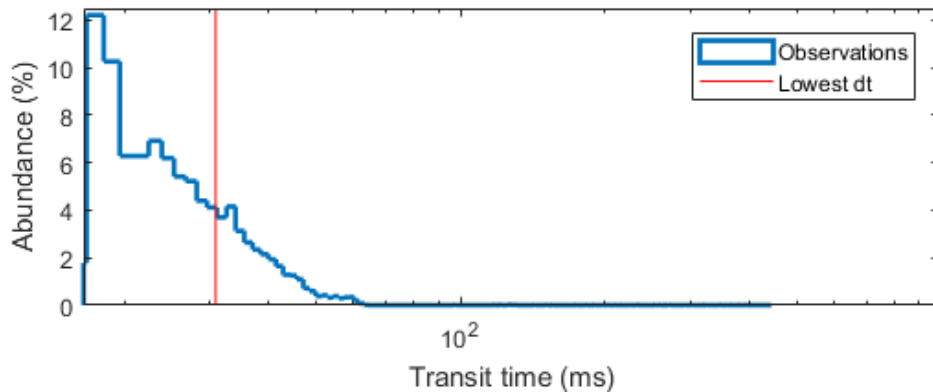

Figure 5.6: *Histogram of transit times (dt). The red line indicates 31.6 ms which is the threshold to measure WBFs as low as 95 Hz.*

During the afternoon of May 16th, bark beetles were released from the trap underneath the lidar transect. Figure 5.7 shows two histograms of observations collected during this time: one of all observations and one of observations which has frequencies lying in the
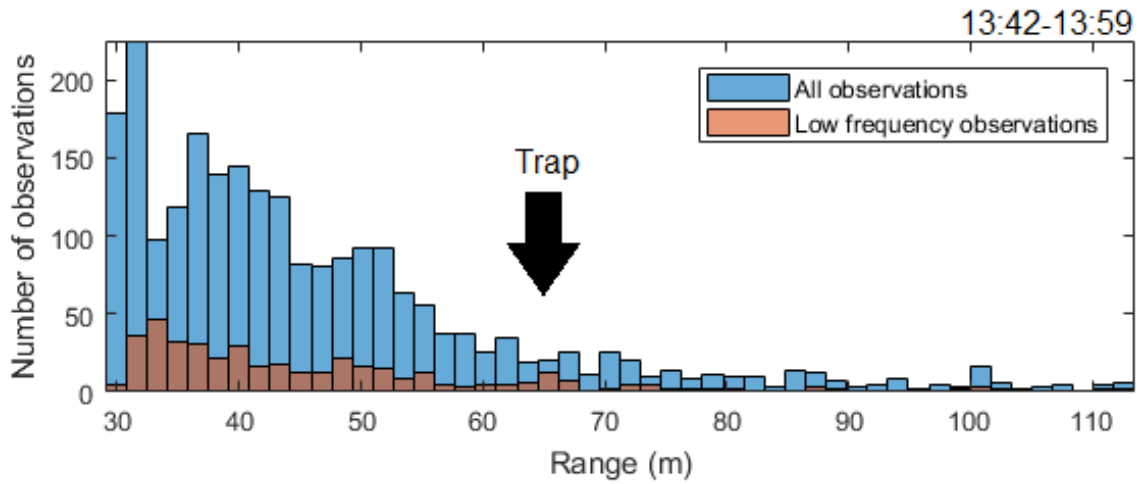
20

Figure 5.7: *Histogram of observations captured at different distances. The low frequency observations indicate observations with frequencies that lay in the bark beetle range.*

bark beetle range ($95\,\text{Hz} < f0 < 145\,\text{Hz}$). The number of observations decrease with range as the laser illumination is weaker. This can be seen in both histograms. There is a small spike in observations in between 60 and 70 m, corresponding to bark beetles flying out from the trap.
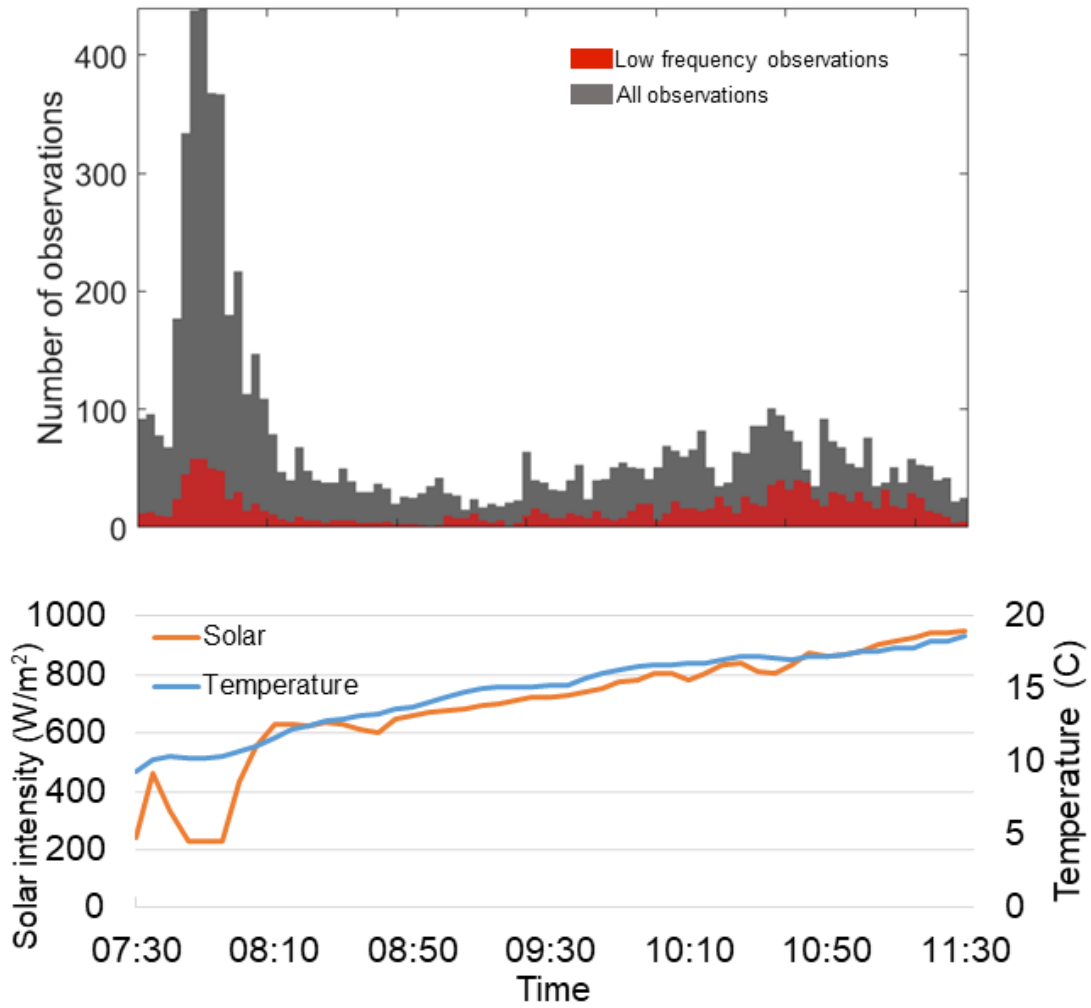
Figure 5.8: *Histogram over all observations, as well as possible bark beetle observations over four hours in the morning of May 16th.*

Figure 5.8 shows a histogram of all observations as well as a histogram of observations with selected WBFs in the bark beetle span, collected over four hours in the morning of May 16th. It also shows temperature and sunlight measured by the weather station during these times. Around 07:50 there is a spike in insect observations. This could be due to the crepuscular behavior of certain insects, notably mosquitoes [28]. The increase over the coming hours show some variability in total observations but lower variability and a steady increase in the lower frequency observations, perhaps suggesting the bark beetle concentrations increase steadily with temperature.
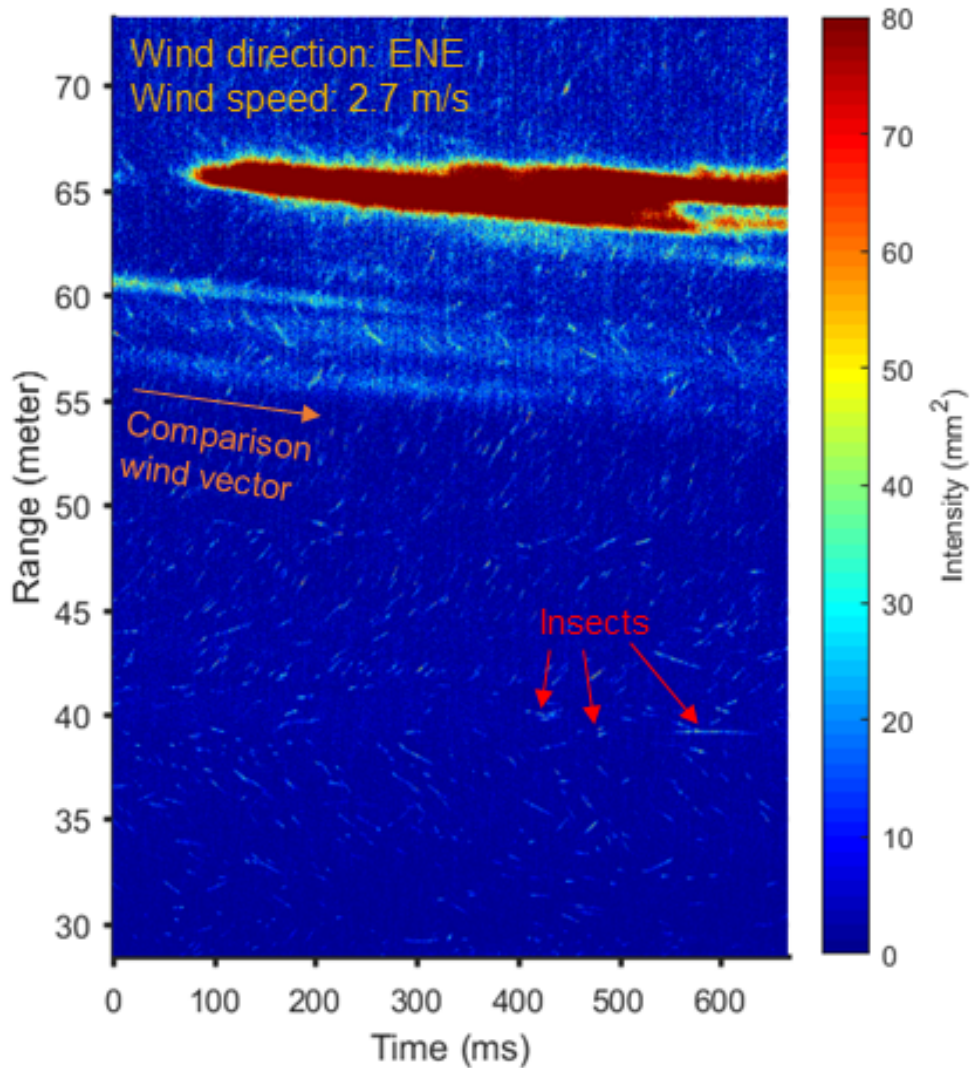
22

5.3 Plume release

Figure 5.9: *Range time map over the ammonium chloride plume*

Figure 5.9 shows a 700 ms time-range map recorded during the ammonium chloride plume release to visualize pheromone transport with the wind. As can be seen the plume is visible at approximately 100 ms and 65 m before dispersing with time. Insect observations are also visible as bright spots on both sides of the plume. At the time of recording, the wind direction as measured by the weather station was approximately parallel with the lidar transect traveling at 2.7 m/s. To compare this a wind vector has been added showing how the wind travels with this velocity.

5.4 Wing thickness

Figure 5.10a shows the specular wing beat part of an observation collected in the ento-
mological test chamber for both wavelengths. To estimate wing thickness, comparisons
between the peak intensities of 11 wing beats have been numbered and plotted against
each other in figure 5.10d,e. Overlayed are intensity ratios from interference patterns of
the two wavelengths, over varying thickness through a thin film. The relative interference
patterns of the two wavelengths are shown in figure 5.10b,c. The color of the thickness
range used, given by the angle, yields a ratio between the interference intensity of two
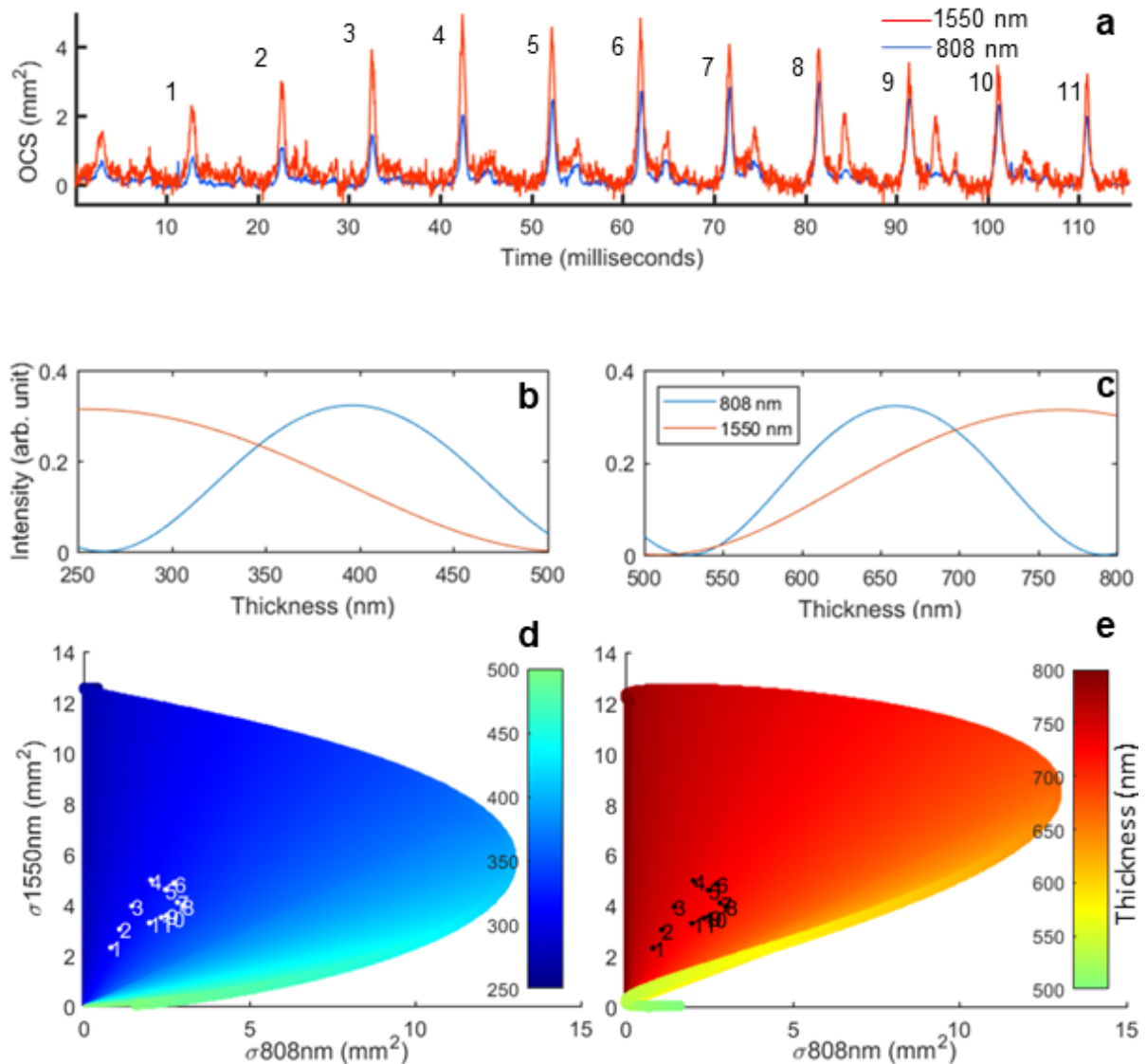wavelengths indicating a thickness.

Figure 5.10: *a) An observation reduced to specular wing beats. b,c) Calculated interference
from two wavelengths through a thin film of varying thickness. c,d) Wing beats overlayed
on interference curves.*

The range of thicknesses were suggested by previous measurements of hyperspectral
images of bark beetle wings and future measurements of more samples will likely give a
more accurate range. Because of the periodic nature of the interference, the total range
was split into two subranges: 250-500 and 500-800 nm. The angles suggest a thickness

24

of either 300-350 or 650-700 nm. This could be avoided in a future reproduction of this experiment by adding a third wavelength, preferably one with a high reflected intensity around 500 nm. Figure 5.11 shows the full range by adding a counter vector that cycles through the range of the interference patterns in the added dimension, showing that the recorded wing thickness ratios cross the interference pattern twice.
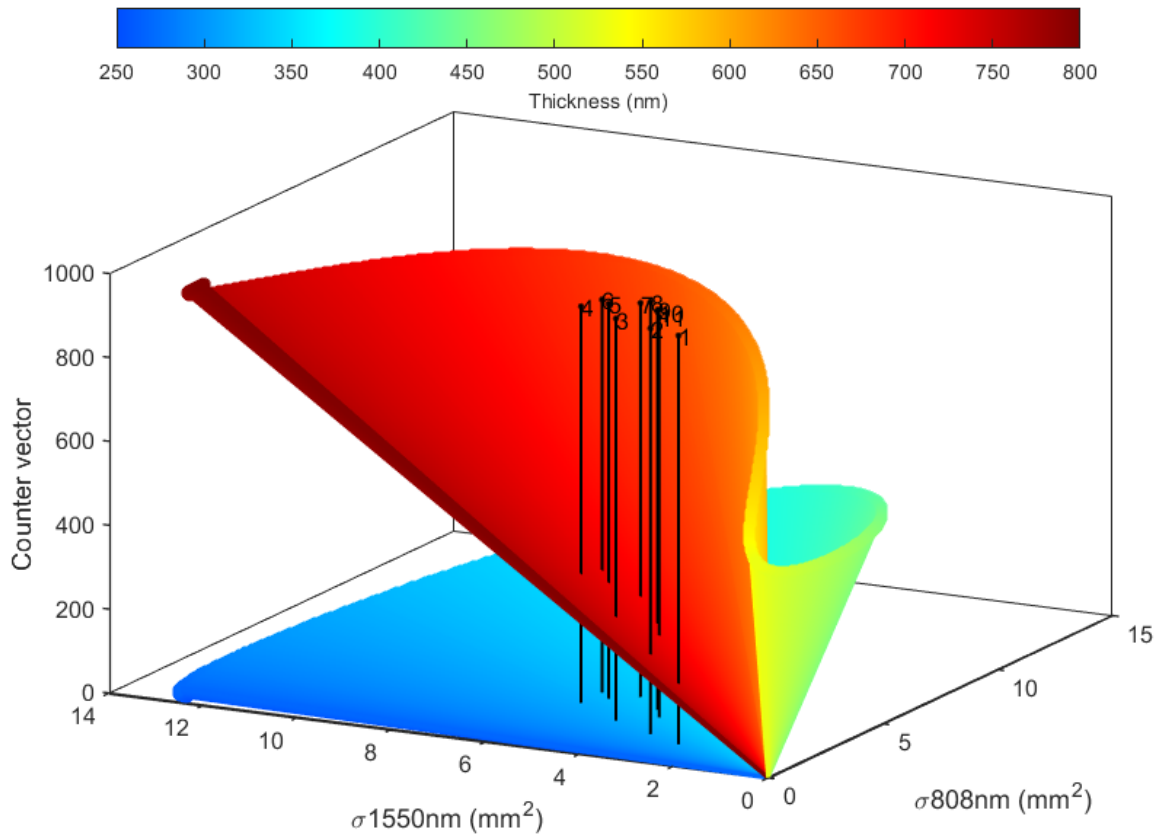

Figure 5.11: *The full thickness range 250-800 nm showing the folding behavior of the two interference patterns.*

6   Conclusion and Outlook

The usage of the parametrization model on bark beetle signals suggests it is possible to measure relative abundances of bark beetle concentrations. Only using the WBF is however a crude method of species determination as there are likely thousands of other species of e.g. beetles which have WBFs in a similar range. It has previously been used on mosquitoes where it works well due to their characteristic high frequencies and matches well with expected diurnal flying behavior. For practical applications where quantitative estimates of bark beetles need to be made, compared to other species, for example in surveying forests for possible outbreaks, more sophisticated methods are most likely needed. Efforts by the company FaunaPhotonics, using artificial neural networks trained on insect signals in realistic field conditions, show promise with high identification rates of e.g. bees and bumblebees with WBFs in a similar range.

The visualization of the ammonium chloride plume shows promise with the current lidar system and could possibly be used in tandem with insect measurements over time to investigate local wind patterns carrying pheromones. Further studies are likely needed on the behavioural effects of ammonium chloride on flying insects to ensure minimal interaction as well as optimal concentration limits and attenuation effects on the laser. Other compounds could also be used as possible sources.

Using specular thin film interference could possibly serve as a reliant method of wing thickness determination with a lidar system capable of polarization separation. Using a third wavelength would give a better estimate by extending the possible thickness range which is cut short due to the folding behavior of two interference patterns. A quantitative measurement of interference measurements could also feasible with information on wing area size. Presently, ongoing work in the research group and the development of a new test chamber with a high speed camera set to trigger on insect detection, gives the possibility of correlating heading with reflected intensity signals. For beetles, species specific information could be gained by comparing different wavelengths of light backscattered from the raised elytra in the forward direction [29].

7   Acknowledgements

Bibliography

[1] 2018 var skogsskadornas år, Skogsaktuellt, https://www.skogsaktuellt.se/artikel/59822/2018-var-skogsskadornas-r.html, Accessed: 2019/11/26.

[2] Narayanan Subramanian, Johan Bergh, Ulf Johansson, Urban Nilsson, and Ola Sallnäs. Adaptation of forest management regimes in southern sweden to increased risks associated with climate change. *Forests*, 7(1):8, 2016.

[3] Granbarkborre, Skogsstyrelsen, https://www.skogsstyrelsen.se/granbarkborre, Accessed: 2019/11/25.

[4] Delade meningar om vinst med fällor, LandSkogsbruk, https://www.landskogsbruk.se/skog/delade-meningar-om-vinst-med-fallor/, Accessed: 2019/11/26.

[5] Jamie Carter, Keil Schmid, Kirk Waters, Lindy Betzhold, Brian Hadley, Rebecca Mataosky, and Jennifer Halleran. Lidar 101: An introduction to lidar technology, data, and applications. *National Oceanic and Atmospheric Administration (NOAA) Coastal Services Center, Charleston, South Carolina, coast. noaa. gov/digitalcoast/_/pdf/lidar101.*, 30, 2012.

[6] Vladimir A Kovalev and William E Eichinger. *Elastic lidar: theory, practice, and analysis methods.* John Wiley & Sons, 2004.

[7] Mikkel Brydegaard, Elin Malmqvist, Samuel Jansson, Jim Larsson, Sandra Török, and Guangyu Zhao. The scheimpflug lidar method. In *Lidar Remote Sensing for Environmental Monitoring 2017*, volume 10406, page 104060I. International Society for Optics and Photonics, 2017.

[8] Elin Malmqvist, Mikkel Brydegaard, Marcus Aldén, and Joakim Bood. Scheimpflug lidar for combustion diagnostics. *Optics express*, 26(12):14842–14858, 2018.

[9] Harold M Merklinger. Principles of view camera focus. *C) May*, 1996.

[10] Liang Mei. Remote sensing of atmospheric aerosol and gas using scheimpflug lidar (slidar) based on diode lasers. In *2016 Progress in Electromagnetic Research Symposium (PIERS)*, pages 3294–3294. IEEE, 2016.

[11] SA Combes and TL Daniel. Flexural stiffness in insect wings i. scaling and the influence of wing venation. *Journal of experimental biology*, 206(17):2979–2987, 2003.

[12] Jiyu Sun and Bharat Bhushan. Structure and mechanical properties of beetle wings: a review. *Rsc Advances*, 2(33):12606–12623, 2012.

[13] Stacey A Combes. Materials, structure, and dynamics of insect wings as bioinspiration for mav s. *Encyclopedia of aerospace engineering*, 2010.

[14] Mikkel Brydegaard and Samuel Jansson. Advances in entomological laser radar. *The Journal of Engineering*, 2019.

[15] Ekaterina Shevtsova, Christer Hansson, Daniel H Janzen, and Jostein Kjærandsen. Stable structural color patterns displayed on transparent insect wings. *Proceedings of the National Academy of Sciences*, 108(2):668–673, 2011.

[16] Daniel E Azofeifa, Humberto J Arguedas, and William E Vargas. Optical properties of chitin and chitosan biopolymers with application to structural color analysis. *Optical materials*, 35(2):175–183, 2012.

[17] Doekele G Stavenga. Thin film and multilayer optics cause structural colors of many insects and birds. *Materials Today: Proceedings*, 1:109–121, 2014.

[18] Mikkel Brydegaard, Alem Gebru, and Sune Svanberg. Super resolution laser radar with blinking atmospheric particles—-application to interacting flying insects. *Progress In Electromagnetics Research*, 147:141–151, 2014.

[19] Mikkel Brydegaard, Alem Gebru, Carsten Kirkeby, Susanne Åkesson, and Henrik Smith. Daily evolution of the insect biomass spectrum in an agricultural landscape accessed with lidar. In *EPJ Web of Conferences*, volume 119, page 22004. EDP Sciences, 2016.

[20] Mikkel Brydegaard. Towards quantitative optical cross sections in entomological laser radar–potential of temporal and spherical parameterizations for identifying atmospheric fauna. *PLoS One*, 10(8):e0135231, 2015.

[21] Elin Malmqvist, Samuel Jansson, Sandra Török, and Mikkel Brydegaard. Effective parameterization of laser radar observations of atmospheric fauna. *IEEE Journal of Selected Topics in Quantum Electronics*, 22(3):327–334, 2015.

[22] Samuel Jansson. Real-time dispersal of malaria vectors in rural africa monitored with lidar. *Unpublished*, 2019.

[23] Teflon balls, https://www.rgpballs.com/en/teflon-ptfe-balls/, Accessed: 2019/12/04.

[24] Alem Gebru, Samuel Jansson, Rickard Ignell, Carsten Kirkeby, Jord C Prangsma, and Mikkel Brydegaard. Multiband modulation spectroscopy for the determination of sex and species of mosquitoes in flight. *Journal of biophotonics*, 11(8):e201800014, 2018.

[25] Alem Gebru, Samuel Jansson, Rickard Ignell, Carsten Kirkeby, and Mikkel Brydegaard. Multispectral polarimetric modulation spectroscopy for species and sex determination of malaria disease vectors. In *CLEO: Applications and Technology*, pages ATh1B–2. Optical Society of America, 2017.

[26] Smith Jim; Hong-Shum Lily. *Food Additives Data Book (2nd ed.)*. 2011, John Wiley & Sons, ISBN 978-1444397734.

[27] DM Unwin and Sarah A Corbet. Wingbeat frequency, temperature and body size in bees and flies. *Physiological Entomology*, 9(1):115–121, 1984.

[28] Masami Shimoda and Ken-ichiro Honda. Insect reactions to light and its applications to pest management. *Applied Entomology and Zoology*, 48(4):413–421, 2013.

[29] L Christoffer Johansson, Sophia Engel, Emily Baird, Marie Dacke, Florian T Muijres, and Anders Hedenström. Elytra boost lift, but reduce aerodynamic efficiency in flying beetles. *Journal of the Royal Society Interface*, 9(75):2745–2748, 2012.